Spin-dependent parameters P_{n000}, D_{n0n0}, K_{n00n}, D_{s0s0}, D_{s0k0}, M_{s0sn}, and M_{s0kn} in pp elastic scattering at 579 MeV

E. Aprile, R. Hausammann,* E. Heer, R. Hess, C. Lechanoine-Leluc, W. R. Leo, S. Morenzoni, Y. Onel, and D. Rapin
Département de Physique Nucléaire et Corpusculaire, University of Geneva, 1211 Geneva 4, Switzerland

S. Mango
Schweizerisches Institut fur Nuklearforschung, 5234 Villigen, Switzerland
(Received 27 December 1982)

The polarization parameter P_{n000}, the two-spin parameters D_{n0n0}, K_{n00n}, D_{s0s0}, and D_{s0k0}, and the three-spin parameters M_{s0sn} and M_{s0kn} have been measured for pp elastic scattering at 579 MeV between 34° and 118° center-of-mass scattering angle. The experiment was performed at SIN using a polarized proton beam, a polarized butanol target, and a polarimeter for the measurement of the polarization of the scattered proton. These data form the basis for a complete experimental determination of the scattering amplitudes.

I. INTRODUCTION

A long-standing problem in physics has been to find a coherent and workable theory which satisfactorily describes all the dynamical features of the N-N interaction at medium energy. Much hope is currently placed on the bag model[1] and in QCD. As it is believed that nucleons are made of quarks and gluons, one is entitled to demand that the whole theory of nucleon forces should be derived from these degrees of freedom. A thorough study of the subject has been made (see detailed review in Ref. 2) but available results are still uncertain. At present, therefore, most information on the N-N interaction still comes from phenomenological parametrizations of the experimental data, e.g., phase-shift analysis (PSA), dispersion relations, and potential models. At medium energy, these approaches are not entirely phenomenological, however, in that they also rely on a certain number of theoretical elements: in the Paris potential,[3] for instance, the long- and medium-range part is carefully derived from the mesonic and isobaric degrees of freedom; only the short-range part is parametrized in a phenomenological form. Although the Paris potential gives an excellent fit to the data up to 425 MeV,[4] PSA are still most commonly and widely used up to 1 GeV. Above the one-pion production threshold the problem becomes more complicated due to the opening of the $pp \rightarrow \pi d$ and $pp \rightarrow \pi NN$ ($\Delta_{33}N$ or $P_{11}N$) channel. Abundant and complete experimental data are becoming available on the two-body inelastic channel.[5] Many theoretical works on single-pion production based on multichannel calculation have been published during the last three years, giving valuable information on inelasticities but not being completely satisfactory.[2] Of course the correct theory must simultaneously explain the observables in all channels.

In such a situation, a purely experimental solution to the elastic N-N problem exists in the so-called "complete" experiment,[6] i.e., the measurement of a sufficient number of observables concerning the reaction at a given energy and angle, such as to allow a complete reconstruction of the amplitudes directly from the data. For pp elastic scattering, this requires[7,8] the measurement of about 12 or more well chosen observables (differential cross section, and, e.g., polarization, spin correlations, etc.) out of a possible 25 at each given angle and energy—a relatively large task. The results, however, would provide unambiguous and completely model-independent information on the scattering amplitudes. They would also provide a rigorous test of current and future theories of the N-N interaction as well as providing fixed anchor points for many of the phenomenological models currently in use.

We have performed such a "complete" experiment for pp elastic scattering at 579 MeV and report here on some of the measurements performed for this purpose. The pp scattering amplitudes reconstructed from these data have already been presented between 66° c.m. and 90° c.m. in Ref. 9 and for smaller angles down to 38° c.m. in Ref. 8. The data set discussed here includes the polarization parameter P_{n000}, the two-spin parameters D_{n0n0}, K_{n00n}, D_{s0s0}, and D_{s0k0}, and the three-spin parameters M_{s0sn} and M_{s0kn}. The choice of these parameters

was based on a detailed study[7] of the requirements for a complete experiment taking into account experimental feasibility as well as mathematical necessity. For example, the three-spin parameters were found to be necessary for an unambiguous reconstruction of the amplitudes at 90° c.m. In addition, these parameters had to be measured to within a certain precision in order to be useful. Typical statistical errors in these data were $\simeq\pm0.01$ for P_{n000}, $\pm(0.01$–$0.02)$ for K_{n00n}, $\pm(0.02$–$0.03)$ for the D, and ±0.05 for the M parameters.

II. PRINCIPLE OF THE EXPERIMENT

The parameters reported in this paper were determined by a measurement of the polarization of the outgoing scattered proton resulting from the elastic scattering of a polarized beam on a polarized target.

The notation used for these spin-dependent parameters, X_{pqik}, is developed in Ref. 10. The indices refer to the polarization directions of the incident and scattered proton, i.e.,

p	along	$(0,s',n,k')$	scattered
q	along	$(0,s'',n,k'')$	recoil
i	along	$(0,s,n,k)$	beam
k	along	$(0,s,n,k)$	target

The 0 index indicates either an unpolarized initial proton or a final proton whose polarization is not analyzed. The laboratory-frame-of-reference axes attached to the incident, scattered, and recoil protons themselves are shown in Fig. 1. Note that the fixed laboratory frame of the apparatus, on the other hand, is defined by the axes $(\hat{X},\hat{Y},\hat{Z})$, where $\hat{Z}$ corresponds to the direction of the incident beam and $\hat{Y}$ to the vertically downward direction. The azimuthal angle of scattering, ϕ, is then defined as

$$\cos\phi=\hat{n}\cdot\hat{Y} \text{ and } \sin\phi=-\hat{X}\cdot\hat{n}\ , \tag{1}$$

i.e., the angle between the normal to the pp scattering plane and the vertical axis in the laboratory. At $\phi=0$, $\hat{n}$ coincides with $\hat{Y}$.

A. Determination of the spin-dependent parameters

In such an experiment, the component of scattered-proton polarization measured along some axis $\hat{p}$ can be shown to be

$$\langle\vec{\sigma}\rangle\cdot\hat{p}=\frac{P_{p000}+\sum_i(P_b)_iD_{p0i0}+\sum_k(P_t)_kK_{p00k}+\sum_{i,k}(P_b)_i(P_t)_kM_{p0ik}}{1+\sum_i(P_b)_iA_{00i0}+\sum_k(P_t)_kA_{000k}+\sum_{i,k}(P_b)_i(P_t)_kA_{00ik}}\ , \tag{2}$$

where the indices i and k run over $(0,s,n,k)$, and P_b and P_t are the beam and target polarizations. Table I shows explicitly the transverse components of the final polarization along $\hat{n}$ and $\hat{s}'$ for a target polarization along $\hat{n}$ and for the three possible beam-polarization orientations (this corresponds to our experimental situation with azimuthal scattering angle $\phi=0$ and with the polarized target field neglected; the more complicated expressions for nonzero ϕ are given later in Sec. V B). Note that the number of

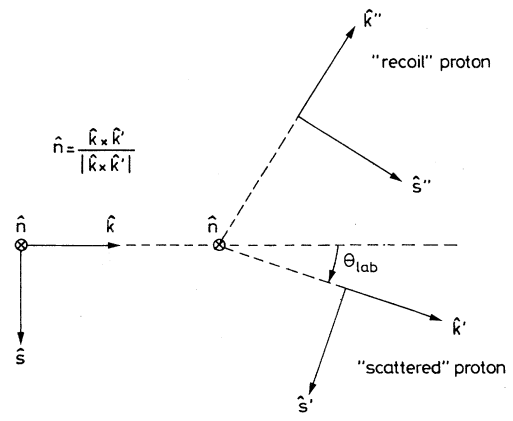

FIG. 1. Laboratory frames attached to the incident, scattered, and recoil protons.

TABLE I. Scattered-proton polarization for the three beam states.

$\hat{P}_b$	$\hat{n}$	$\hat{s}'$
$\hat{Y}$	$\dfrac{P(1+P_bP_t)+D_{n0n0}P_b+K_{n00n}P_t}{1+A(P_b+P_t)+A_{00nn}P_bP_t}$	0
$\hat{X}$	$\dfrac{P+K_{n00n}P_t}{1+AP_t}$	$\dfrac{P_b[D_{s'0s0}+M_{s'0sn}P_t]}{1+AP_t}$
$\hat{Z}$	$\dfrac{P+K_{n00n}P_t}{1+AP_t}$	$\dfrac{P_b[D_{s'0k0}+M_{s'0kn}P_t]}{1+AP_t}$

spin-dependent parameters is reduced as compared to all possible combinations of indices due to parity conservation. Moreover the Pauli principle requires that $A_{00n0}=A_{000n}\equiv A$, $P_{n000}=P_{0n00}\equiv P$, and $A=P$ if time-reversal invariance is assumed. We have also made use of invariance under reflection in the scattering plane (the so-called Bohr's rule[11]) which requires $M_{n0nn}=P$.

To determine the spin-dependent parameters, advantage was taken of the fact that the spin-correlation parameters in the denominator had already been measured[12] in a previous experiment. With this information, and a measurement of $\langle\vec{\sigma}\rangle\cdot\hat{n}$ and $\langle\vec{\sigma}\rangle\cdot\hat{s}'$ for the different beam-target combinations, i.e., $P_b=(\pm X,\pm Y,\pm Z)$ and $P_t=(\pm Y)$, sufficient information was provided to allow an extraction of the parameters in the numerators.

It might be noted here that a measurement of the three-spin parameters using Eq. (2) is always accompanied by a measurement of the two-spin quantities and the polarization parameter P. The higher the spin rank of a parameter, the smaller its determination factor. The relative precision of the three-spin parameters will, thus, always be less than those of the two-spin parameters and these, in turn, less than the polarization parameter.

B. Measurement of the scattered-proton polarization

To measure the polarization of the scattered proton pC scattering was chosen as the analyzing reaction. The outgoing proton was thus allowed to scatter a second time from a carbon target and the polar and azimuthal scattering distributions observed. The form of this distribution is given by

$$\frac{d\sigma}{d\Omega_C}=\sigma_C(\theta_C)\left[1+A_C(\theta_C)\sum_{p=s',n,k'}\langle\vec{\sigma}\rangle\cdot\hat{p}\,\hat{p}\cdot\hat{n}_C\right], \tag{3}$$

where $A_C(\theta_C)$ is the carbon analyzing power at the pC scattering energy, $\sigma_C(\theta_C)$ is the unpolarized pC scattering cross section, and $\hat{n}_C$ the normal to the plane of the pC scattering. From this expression, it can be seen also that only the transverse components can be measured since the longitudinal direction $\hat{k}'$ is always orthogonal to $\hat{n}_C$.

If we now define the azimuthal carbon scattering angle ϕ_C,

$$\cos\phi_C=\hat{n}\cdot\hat{n}_C \text{ and } \sin\phi_C=-\hat{s}'\cdot\hat{n}_C\,, \tag{4}$$

Eq. (3) then becomes

$$\frac{d\sigma(\theta_C,\phi_C)}{d\Omega_C}=\sigma_C(\theta_C)[1+A_C(\theta_C)P_n\cos\phi_C - A_C(\theta_C)P_{s'}\sin\phi_C]\,, \tag{5}$$

where P_n ($\equiv\langle\vec{\sigma}\rangle\cdot\hat{n}$) and $P_{s'}$ ($\equiv\langle\vec{\sigma}\rangle\cdot\hat{s}'$) are the $\hat{n}$ and $\hat{s}'$ polarization components of the scattered proton [see Eq. (2) and Table I]. A statistical analysis of the measured distributions with Eq. (5), then yields the quantities

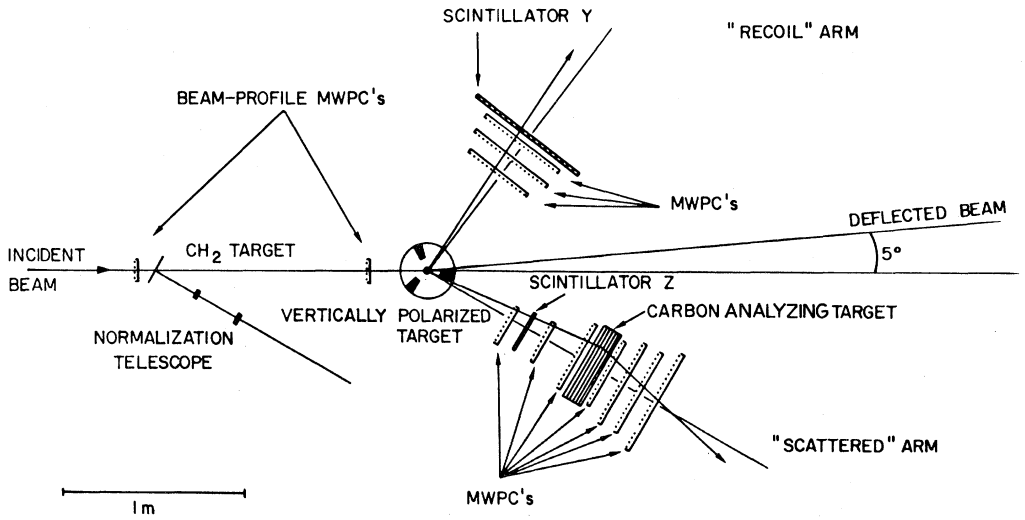

FIG. 2. Experimental setup viewed from top.

$$\epsilon_n(\theta_C)=A_C(\theta_C)P_n\ ,$$
$$\epsilon_{s'}(\theta_C)=-A_C(\theta_C)P_{s'}\ , \tag{6}$$

which are the two asymmetries governing the distribution. With a knowledge of A_C, P_n and $P_{s'}$ can be fitted and determined as described before. With these measurements in view, therefore, the carbon analyzing power in the energy-angle range appropriate to the outgoing proton were measured in a previous experiment.[13,8]

III. EXPERIMENTAL APPARATUS AND TECHNIQUE

In this section we will present a brief summary of the experimental setup. A complete description may be found in Ref. 14 for those who desire more detail.

A. The polarized proton beam

These measurements were carried out at the SIN PM1 beam line using, in part, the "scattered" polarized proton beam, and, in part, the "accelerated" beam. In the "scattered-beam" mode, polarized protons were produced by an 8° scattering of the main unpolarized beam from an 8-mm-thick Be target just before injection into the PM1 channel. The polarization obtained was measured[15] at $|\vec{P}_b|=0.4165\pm0.0043$ with the spin vector pointing vertically downward. To change the direction of this vector, a combination of two superconducting solenoids sandwiching the last deflection was used to precess the proton spins. Orientations in the transverse ($\hat{X}$) and longitudinal ($\hat{Z}$) directions, as well as complete spin flips were accomplished in this manner.

While the majority of the data were taken with this beam, a small fraction was also taken in the "accelerated-beam" mode. Here, polarized protons were produced by a "ground-state atomic-beam" source and accelerated to full energy by the SIN cyclotron. Much higher polarizations, typically on the order of 0.8 were obtained; however, a constant monitoring of this polarization was necessary. This was performed by a small CH_2 polarimeter located in the beam channel. Periodic spin flips could also be performed directly at the ion source allowing a better control of systematic errors. Reorientation of the polarization vector, however, was performed in the same manner as for the scattered-beam mode. Typical intensities for these measurements were a few 10^7 protons/sec.

B. Detector layout

A schematic diagram of the detector layout is shown in Fig. 2. The beam intensity was monitored by a small scintillation-counter telescope which detected the number of protons scattered from a 5-mm-thick polyethylene target located in the beam. This number was used for the subtraction of background events measured with a dummy target. The position and profile of the beam were also monitored by two small multiwire proportional chambers (MWPC's) designed for high intensity.

The scattered and recoil protons emerging from the polarized proton target (PPT) were detected by two X-Y telescopes each consisting of three multiwire proportional chambers and a scintillation counter. Each telescope was mounted on a movable platform which could be rotated about the target axis as to allow easy access to different angular ranges.

To measure the spin polarization of the scattered proton, a polarimeter was mounted directly behind the "scattered" proton telescope. This consisted of a series of carbon plates followed directly by four MWPC's. By adding or removing plates, the thickness of this carbon target could be varied from 1 to 7 cm so as to allow an optimization with respect to the energy of the scattered proton. In order to ensure a good efficiency for detecting scatterings from the carbon, four chambers were used.

This setup covered with a single detector-arm position an angular acceptance of $\Delta\theta_{\text{c.m.}}=\pm16°$ and $\Delta\phi=\pm10°$ for the first scattering.

For the second scattering, events falling in θ_C cones up to the full opening of interest (20° lab) were accepted within $\Delta\theta_{\text{c.m.}}=\pm10°$. For larger angles $\theta_{\text{c.m.}}$ the θ_C cones were reduced linearly to about 12° lab at $\Delta\theta_{\text{c.m.}}=\pm16°$. These measurements between 118° c.m. and 34° c.m. were taken with three different arm positions at 104° c.m., 80° c.m., and 48° c.m., corresponding to 41°, 30° and 16° lab for the "scattered" arm.

1. Chamber alignment

The MWPC's in each of the two telescopes were aligned with the aid of the proton beam and three scintillation counters carefully positioned along the theoretical beam line. Each telescope was placed in the beam defined by these counters and the positions of the beam profile in each of the chambers relative to two reference chambers measured. If the displacement was greater than 1 mm, the chamber was physically repositioned. Any remaining displacements were then recorded on a disk file and used to correct the measured coordinates during data acquisition.

For the polarimeter, misalignments were more crucial, however, because of the false asymmetries which they can produce. To eventually correct for

this possibility, special data were taken during the acquisition. This is described in Sec. IV A.

C. The polarized proton target (PPT)

The polarized target consisted of frozen beads of butanol $CH_3(CH_2)_2CH_2OH$ immersed in liquid ^3He at a temperature of 0.5° K. This sample was placed in a vertical magnetic field of 25 kG and polarized by the method of dynamic nuclear orientation. The polarization was monitored continuously by a NMR technique, with typical values of P_t being about 40–60 %. This target is the same as that used in a previous measurement[12] and we refer the reader there for further details.

In order to take into account background reactions occurring on the C, ^3He, and O atoms in the PPT, measurements were taken with a dummy target consisting of a copper cylinder of the same size, filled with carbon grains of a few millimeters diameter immersed in liquid ^3He. The relative amounts of carbon and ^3He were adjusted so as to give the same ratio of C + O to ^3He as in the butanol target. Oxygen, here, was counted as an extra carbon atom. The total number of atoms in this dummy target, however, was greater than that in the PPT by a factor $\simeq 1.5$. Background data from these measurements were therefore normalized by this factor as well as by the total number of incident particles.

To facilitate the background measurements, the dummy target was mounted directly underneath the butanol cavity to form a two-stage PPT. Either cavity could then be placed into the beam by simply sliding the supporting central stem up or down in the cryostat. Of course during this operation, the cryostat itself and the coils for the magnetic field were kept untouched.

D. The electronic system and logic

The system shown in Fig. 2 was CAMAC controlled by a PDP 11/20 computer which managed and coordinated system operations during data acquisition. Besides the actual data taking, this included a periodic monitoring of the operational parameters of the system, such as the MWPC and photomultiplier voltages, current in the solenoid, etc.

Triggering of the detection system was produced by the coincidence $Y*Z$, which indicated a possible scattering event on the PPT. This signal was used to set the system BUSY and initiate memorization and coding of the MWPC information. Since the probability for a proton to undergo a double scattering is very low ($\simeq 10^{-5}$), an event selection had to be performed. This was done by sending the information to a special hardware central unit (CU) which counted the number of hits in each MWPC plane and, based on the slopes of the trajectories, decided if a second scattering on the carbon had occurred. Furthermore, to facilitate event reconstruction, the CU made certain that there was one and only one single hit in two out of three planes (or in two out of four in the rear polarimeter telescope) per coordinate and telescope. Events failing to meet this requirement were immediately rejected and the system reset. Typical decision times for this CU unit were on the order of 5 μsec. If the event was accepted, the CU issued a LAM signal to the PDP 11/20 which then transferred the MWPC information to a specially made minicomputer DPNC 811 with 56-kbyte capacity for event reconstruction. Typical transfer times were $\simeq 1$ msec/event.

The DPNC 811 had a performance equivalent to that of a PDP 11/45 and was entirely dedicated to event reconstruction and the storage of data. This procedure is described in the next section. To speed up event reconstruction, two DPNC 811's were used in parallel during the actual experiment. The registered event was then sent to whichever of the two DPNC 811's was free at the moment.

IV. DATA ACQUISITION

A. Types of events

The data for this measurement were accumulated over two separate periods of about one month each. In each case, essentially three types of data were taken.

1. Double-scattering events

Double-scattering events were accumulated for 22 angular bins in $\theta_{c.m.}$ between 34° and 118°. To cover this range three arm positions were used with some overlap. The azimuthal ϕ range accepted in all three cases was ±10°. Data were taken for the beam and target configurations, $P_b(\pm X, \pm Z)$ and $P_t(\pm Y)$ and in some cases $P_b(\pm Y)$ and $P_t = 0$. About 20×10^3 events per $\theta_{c.m.}$ bin per beam-target condition were taken.

2. Background data

Background data taken with the dummy target were accumulated alternatively with the butanol runs. About $\frac{1}{4}$ of the running time was spent on this phase.

3. Straight-through events

In addition to the above data, unscattered "straight-through" events in the polarimeter with

and without the carbon target were periodically accumulated to be used in the off-line analysis for correcting chamber misalignments. The straight-through events without carbon target were accumulated in separate dedicated runs several times during a run period. The straight-through events, with carbon however, were taken alternatively with the double-scattering data during a run. The data-acquisition program spent about 20% of the time on the accumulation of these data.

B. On-line event reconstruction

To diminish dead time and magnetic tape wasted on recording bad events, a fast on-line reconstruction procedure was used as an event filter. Only events which passed through a series of loose cuts placed on these reconstructed parameters were then recorded on magnetic tape for later analysis off-line. The same reconstruction procedure was then used but with more stringent cuts.

The on-line reconstruction consisted of two distinct parts: (1) the reconstruction of the *pp* scattering parameters and (2) the reconstruction of the carbon analyzing scattering in the polarimeter. For each part, a different method had to be used.

The total time for both the first and second reconstructions was on the order of 5 msec. To speed up processing, two DPNC 811 were used in parallel allowing a total of about 300 events/sec to be treated. Of these, only about 8% ($\simeq$25/sec) were finally accepted and stored in the magnetic tape.

1. Reconstruction of the first scattering on the PPT

For each scattering event on the PPT, the coordinates of the scattering vertex x_v, y_v, and z_v, the center-of-mass polar and azimuthal scattering angles $\theta_{\text{c.m.}}$ and ϕ, and the vertically projected slope α_v of the incident proton were reconstructed from the MWPC coordinates of the scattered and recoil telescopes using a matrix technique which we will only summarize here. For a more detailed description, the reader is referred to Ref. 16. These MWPC coordinates were obtained from the recorded tracks after subtraction of offsets due to chamber displacements and an alignment test for each coordinate in the two telescopes.

Basically, the method consists of linearizing the relation between the MWPC coordinates and the scattering parameters. Grouping the corrected MWPC coordinates into a vector $\vec{X}$ and the reaction parameters (i.e., the scattering angles, vertex, etc.), into a vector $\vec{P}$, this relation is

$$\vec{X}=\vec{F}(\vec{P}) , \tag{7}$$

where the function $\vec{F}$ essentially describes the trajectory of the particles through the target and detection systems. The exact form of $\vec{F}$ thus depends on the particles involved, the geometry of the apparatus, the presence of absorbing materials, magnetic fields, etc., and is, in general, a rather complicated function. Over a limited range of scattering angles, however, $\vec{F}$ can be approximated by a first-order expansion about some central parameter value $\vec{P}_0$, i.e.,

$$\vec{X}\simeq\vec{F}(\vec{P}_0)+\left.\frac{\partial\vec{F}}{\partial\vec{P}}\right|_{\vec{P}_0}(\vec{P}-\vec{P}_0)=\vec{X}_0+\underline{D}(\vec{P}-\vec{P}_0) , \tag{8}$$

where $\vec{X}_0\equiv\vec{F}(\vec{P}_0)$ are the central coordinates and $\underline{D}$, the constant matrix of first derivatives $\partial\vec{F}/\partial\vec{P}$ evaluated at $\vec{P}_0$. If we now define the "reduced" coordinates and parameters, $\vec{x}=(\vec{X}-\vec{X}_0)$ and $\vec{p}=(\vec{P}-\vec{P}_0)$, Eq. (7) can be rewritten as

$$\vec{x}=\underline{D}\vec{p} . \tag{9}$$

This may now be used for event reconstruction by substituting in the measured $\vec{x}$. Equation (9) then becomes a system of overdetermined equations (since there are more MWPC coordinates than parameters to be reconstructed) for $\vec{p}$. This may be inverted by a least-squares method to give the "reconstruction" matrix, $\underline{R}$,

$$\vec{p}=(\underline{D}^t\underline{G}\,\underline{D})^{-1}\underline{D}^t\underline{G}\vec{x}=\underline{R}\vec{x} , \tag{10}$$

where $\underline{D}^t$ is the transpose of the matrix $\underline{D}$. In this procedure, we have also added a weight matrix $\underline{G}$, which is equal to the inverse of the covariance matrix of the measured MWPC coordinates. This constant matrix essentially accounts for the finite resolving power of the detection apparatus. Event reconstruction with Eq. (10) is thus reduced to a very simple (and fast) multiplication of the recorded MWPC coordinates by a constant matrix $\underline{R}$.

In these experiments, the matrices $\underline{D}$, $\underline{G}$, and $\underline{R}$ were all calculated beforehand on a CDC 170 computer using a tracking program which determined in detail the trajectories of the protons as they passed through the detection system. The weight matrix $\underline{G}$ was calculated taking into account the spatial resolution of the MWPC's ($\simeq$0.6 mm), the dispersion in the incident beam momentum (0.325°, 6 MeV/c) and multiple scattering in the system. From this, the resulting overall angular resolution of the system was found to be about 1° for the c.m. scattering angle $\theta_{\text{c.m.}}$. All these matrices information were then loaded into the memories of the DPNC 811 for use by the on-line reconstruction program during data

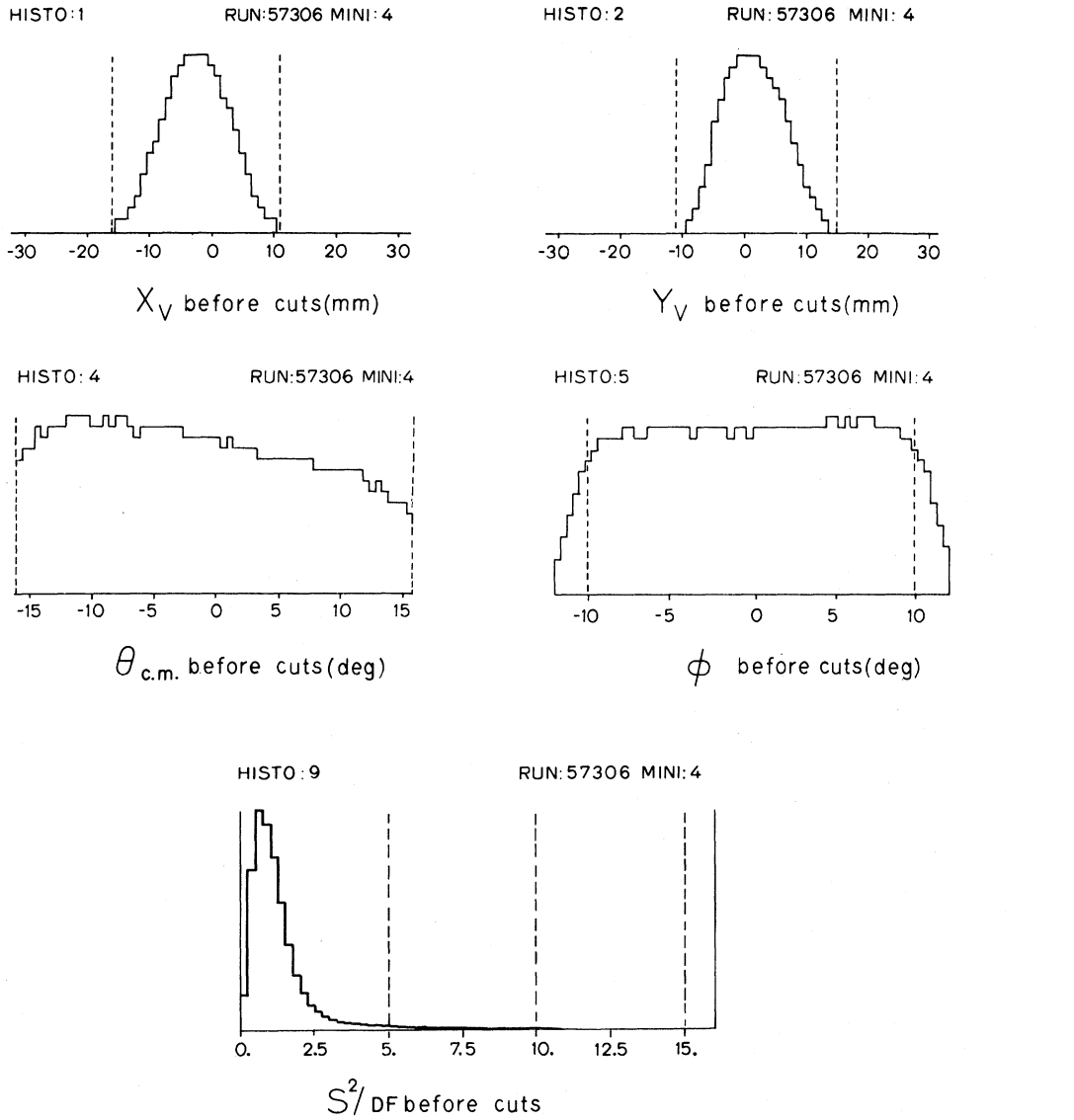

FIG. 3. Sample histograms for the *pp* elastic scattering.

acquisition. The necessity of preparing these matrices before the actual measurement also proved to be particularly advantageous since it also allowed a preview of certain characteristics of system performance, for example, the resolution and acceptance.

In order to judge the quality of reconstruction, a "goodness-of-fit" parameter S^2 could also be calculated for each event by taking the difference between the measured MWPC coordinates $\vec{x}$ and the "theoretical" MWPC coordinates $\vec{x}_r$ as determined from the reconstruction parameters $\vec{p}=\underline{R}\vec{x}$, i.e.,

$$S^2=(\vec{x}-\vec{x}_r)^t\underline{G}(\vec{x}-\vec{x}_r)\,, \tag{11}$$

where $\vec{x}_r=\underline{D}\vec{p}=\underline{D}\,\underline{R}\vec{x}$. If $\vec{x}$ has a Gaussian-type distribution (which proved to be the case in this experiment), then, it can be shown that S^2 follows a χ^2 distribution with, in our case, six degrees of freedom. This allows a statistical decision to be made and thus a means of rejecting background or other bad events.

The method as described up to now is valid, of course, only as long as the linear approximation in Eq. (8) holds. In practice, the angular range of interest in these measurements was somewhat larger than the range of validity of Eq. (8), so that non-negligible "nonlinearities" [i.e., errors due to the negligence of higher, nonlinear terms in Eq. (8)] would occur in the event reconstruction, especially for events far from the central parameters. This problem could be solved, however, by readjusting the

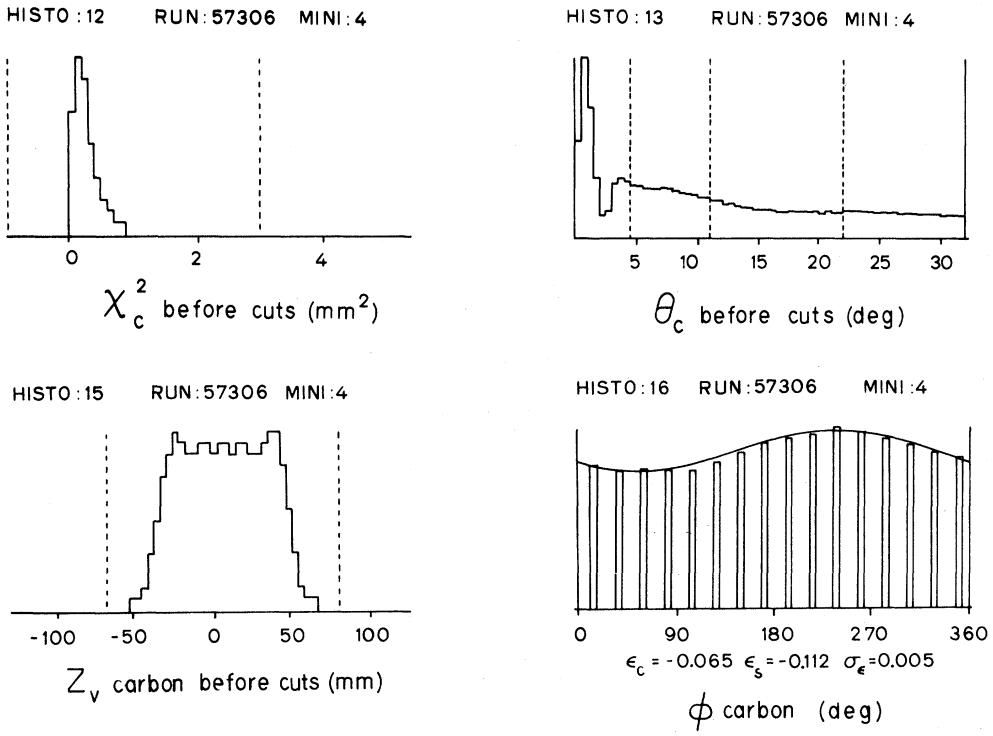

FIG. 4. Sample histograms from polarimeter processing.

measured coordinates with a correction, $\Delta\vec{x}$. These corrections were computed by the generation program in tabular form as a function of the reconstructed $\theta_{c.m.,r}$ and ϕ_r, and loaded into the DPNC 811 along with the matrices. A first reconstruction was then made with the raw "MWPC" coordinates which provided the $\theta_{c.m.,r}$ and ϕ_r values. The correction was then "looked up," applied to the measured coordinates which were then passed through the reconstruction a second time to give the corrected reconstructed parameters. If the event fell outside the range of the table being a bit larger than our measured range, the event was immediately rejected. This criterion, in fact, proved to be quite powerful accounting for about 30% of the rejections.

In addition, to the above matrices, a list of cuts on p was also loaded into the DPNC 811 and supplied to the on-line reconstruction program for use in rejecting events. These cuts were kept relatively large so as to ensure acceptance of all good events. Roughly 30% of all events were accepted with these limits. The accepted data were recorded on magnetic tape for off-line analysis where more stringent cuts were used. In addition, the matrix-reconstructed information was put to further use by storing it in the DPNC 811 memory in the form of histograms. This provided a set of "control" histograms which could be displayed at any time during the acquisition together with further information about the system's performance. This allowed an immediate and very complete monitoring of the running acquisition. Figure 3 shows some typical examples. The vertex distributions are resolved to within a few mm and are stable to within $\simeq$2 mm. Examples of $\theta_{c.m.}$, ϕ, and S^2 per degree of freedom are also shown. Note the resemblance of S^2 to a true χ^2.

Missing and Spurious Tracks. In order for the matrix method to work, each event must have a full set of MWPC coordinates $\vec{X}$. During an actual experiment, of course, this is not always the case, since missing or extra spurious tracks occasionally occur due to the inefficiencies of the MWPC's. In this experiment, only one missing or spurious track per projection in each telescope could be tolerated and still allow an event reconstruction. In such a case, the missing coordinate was generated by extrapolation of the straight line formed by connecting the two recorded tracks. In the reconstruction this was taken into account by reducing the degrees of freedom accordingly. In the case of spurious tracks, the two recorded coordinates were tested for alignment with the other tracks and the best one taken.

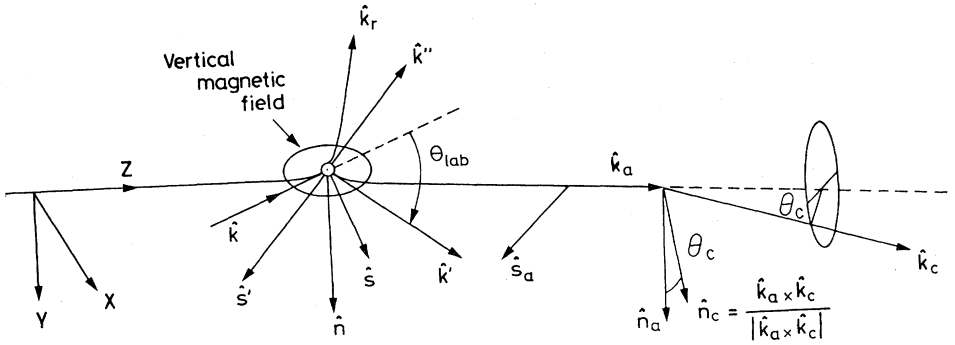

FIG. 5. Double scattering with magnetic field.

2. Reconstruction of the analyzing scattering on carbon

Because of the large angular range of interest ($\phi_C = 0 \rightarrow 2\pi$) for the analyzing scattering on carbon, a matrix technique could not be used for this part of the reconstruction. Instead, a more conventional on-line method was employed. This proceeded as follows.

(1) The incident track on the carbon analyzing target was first reconstructed from the MWPC coordinates $\vec{X}$.

(2) The scattered track was then tested for reconstructibility by checking the alignment of the four MWPC coordinates. A χ^2 with respect to the best-fitting straight line was calculated and a cut was applied (see vertical line in Fig. 4).

(3) Next, the polar scattering angle θ_C was calculated. Events whose θ_C was too small ($\theta_C < 5°$) or too large to allow acceptance of a full cone in ϕ_C by the polarimeter were rejected. In Fig. 4 one notices for angles below 5° a suppression of events due to the central decision unit (CU). But this unit was not 100% efficient as it was not able to calculate the scattering angle when inefficiencies or parasites occurred in two out of the three first chambers in the rear telescope.

(4) The squared distance of closest approach between the incident and scattered tracks, d^2, was then calculated. All events with $d^2 > 15$ mm^2 were rejected.

(5) The scattering-vertex coordinate z_C in the carbon was calculated. Figure 4 shows a typical histogram of this parameter. One can vaguely discern the carbon plates which indicates a resolution of a few mm. All events, of course, were restricted to the carbon region.

(6) Finally, the azimuthal scattering angle ϕ_C was calculated (see Fig. 4). The computed asymmetries (integrated over θ_C) gave an immediate check of the beam-polarization direction, i.e., to detect a solenoid failure.

A rejection at any stage of this procedure, of course, halted all further processing of the event in order to save time. The largest rejections occurred at level (3) where $\simeq$60% of the events failed to pass. The overall acceptance of the polarimeter reconstruction was $\simeq$20%.

V. DATA ANALYSIS

In the off-line analysis, events were passed once more through the matrix reconstruction program but with more stringent cuts and after having corrected the measured MWPC coordinates for misalignments in the MWPC's. These global displacements have been evaluated using the straight-through events recorded without carbon target. Choosing two reference chambers and assuming perfectly parallel wires with equal spacing in each plane, these data allowed the determination of one transverse displacement, ΔX or ΔY, the longitudinal displacement ΔZ, and the rotational misalignments $\Delta\phi_X$, $\Delta\phi_Y$, and $\Delta\phi_Z$ about the X, Y, and Z axes, respectively. These corrections were then applied directly to the raw MWPC coordinates before reconstruction. Accepted events were accumulated into sums (see Sec. V A 2) in order to find the transverse scattered-proton polarizations from which the spin-dependent parameters are extracted (see Sec. V B). The overall angular range at the PPT scattering was divided into five bins in azimuthal angle ϕ, eight bins in $\theta_{c.m.}$, and two bins in S^2.

A. Evaluation of the scattered-proton polarization

This evaluation, however, was complicated by several factors: (1) the effect of the magnetic field of the PPT, (2) instrumental asymmetries due to chamber misalignments, and (3) contaminating background reactions. The treatment of these effects is discussed below.

1. *Effect of the PPT magnetic field*

The 25-kG magnetic field of the polarized target perturbed the spin polarization measurements in two ways: (1) by precessing the proton spin and (2) by deflecting the proton trajectories. Figure 5 shows the situation schematically for the case $\phi=0$, i.e. $(\hat{Y}||\hat{n})$, the deflection due to the magnetic field being greatly magnified. The incoming proton is slightly deflected and its spin precessed in the first half of the field. Assuming the reaction takes place at the target center, the polarization $\vec{P}$ of the scattered proton can be expressed in the $(\hat{s}',\hat{n},\hat{k}')$ frame as

$$\vec{P}=P_{s'}\hat{s}'+P_n\hat{n}+P_{k'}\hat{k}' . \tag{12}$$

Since the PPT magnetic field precesses $\vec{P}$ by a rotation R, after the field this polarization becomes

$$R\vec{P}=P_{s'}R\hat{s}'+P_nR\hat{n}+P_{k'}R\hat{k}' . \tag{13}$$

Letting $\hat{k}_a$ be the direction of the scattered proton after the magnetic field, we note that neither $\hat{k}'$ nor $R\hat{k}'$ is parallel to $\hat{k}_a$ since the magnetic rotation for a trajectory is different from that for a polarization. Since the second scattering on carbon can only determine the transverse polarization of the proton, it is necessary to choose two orthogonal axes $\hat{s}_a$ and $\hat{n}_a$ perpendicular to $\hat{k}_a$ for the definition of ϕ_C (see Sec. II B):

$$\cos\phi_C=\hat{n}_a\cdot\hat{n}_C,\quad \sin\phi_C=-\hat{s}_a\cdot\hat{n}_C \tag{14}$$

with the normal to the pC scattering plane given by

$$\hat{n}_C=(\hat{k}_a\times\hat{k}_C)/|\hat{k}_a\times\hat{k}_C| . \tag{15}$$

The measured polarization components will then be

$$\begin{aligned} R\vec{P}\cdot\hat{s}_a&=P_{s'}R\hat{s}'\cdot\hat{s}_a+P_nR\hat{n}\cdot\hat{s}_a+P_{k'}R\hat{k}'\cdot\hat{s}_a ,\\ R\vec{P}\cdot\hat{n}_a&=P_{s'}R\hat{s}'\cdot\hat{n}_a+P_nR\hat{n}\cdot\hat{n}_a+P_{k'}R\hat{k}'\cdot\hat{n}_a . \end{aligned} \tag{16}$$

The relative fractions of $P_{s'}$, P_n, and $P_{k'}$ analyzed are thus determined by the projections, $R\hat{s}'\cdot\hat{s}_a$, $R\hat{s}'\cdot\hat{n}_a$, . . . , etc., which, in general, depend on the scattering angles, $\theta_{c.m.}$ and ϕ as well as on the choice of the analyzing axes $\hat{s}_a$ and $\hat{n}_a$. A good choice for the $\hat{s}_a$ and $\hat{n}_a$ axes is

$$\begin{aligned} &\hat{n}_a \text{ parallel to } \hat{k}_a\times R\hat{s}' ,\\ &\hat{s}_a=\hat{n}_a\times\hat{k}_a , \end{aligned} \tag{17}$$

in order to have the projection $R\hat{s}'\cdot\hat{n}_a=0$ in Eq. (16).

TABLE II. Results for pp elastic scattering at 579 MeV for spin-dependent parameters $D_{\omega 0s0}$, $D_{\omega 0k0}$, $M_{\omega 0sn}$, and $M_{\omega 0kn}$. Numerical values for the mixing angle ω are given in last column. Quoted errors are purely statistical.

$\theta_{c.m.}$ (deg)	$D_{\omega 0s0}$	$D_{\omega 0k0}$	$M_{\omega 0sn}$	$M_{\omega 0kn}$	ω (deg)
34	0.614±0.035	−0.019±0.037	0.520±0.074	−0.248±0.068	7.53
38	0.657±0.028	0.048±0.030	0.551±0.060	−0.191±0.055	7.59
42	0.666±0.027	0.071±0.028	0.461±0.056	−0.178±0.051	7.64
46	0.650±0.026	0.219±0.027	0.316±0.054	0.026±0.049	7.70
50	0.691±0.025	0.239±0.026	0.371±0.052	−0.025±0.048	7.76
54	0.662±0.024	0.277±0.025	0.282±0.050	0.085±0.046	7.81
58	0.638±0.023	0.328±0.024	0.244±0.049	0.109±0.044	7.87
62	0.640±0.024	0.384±0.025	0.212±0.051	0.139±0.046	7.99
66	0.613±0.026	0.359±0.030	0.127±0.046	0.157±0.056	8.11
70	0.555±0.024	0.409±0.027	0.079±0.043	0.310±0.051	8.22
74	0.568±0.023	0.347±0.027	0.034±0.042	0.284±0.050	8.34
78	0.558±0.023	0.305±0.026	0.014±0.040	0.377±0.048	8.45
82	0.484±0.022	0.274±0.025	−0.034±0.040	0.269±0.048	8.62
86	0.494±0.021	0.256±0.025	−0.041±0.038	0.277±0.047	8.80
90	0.423±0.021	0.249±0.024	−0.130±0.038	0.441±0.046	8.97
94	0.475±0.023	0.127±0.026	−0.089±0.041	0.378±0.050	9.21
90	0.481±0.021	0.230±0.022	−0.136±0.042	0.355±0.040	
94	0.434±0.019	0.132±0.020	−0.126±0.039	0.293±0.037	
98	0.433±0.018	0.086±0.019	−0.099±0.038	0.334±0.036	9.50
102	0.384±0.018	0.056±0.019	−0.116±0.037	0.351±0.035	9.78
106	0.367±0.018	−0.008±0.019	−0.088±0.038	0.232±0.035	10.07
110	0.391±0.019	−0.042±0.020	−0.123±0.039	0.200±0.037	10.49
114	0.353±0.021	−0.061±0.021	−0.179±0.042	0.262±0.039	10.89
118	0.353±0.028	−0.096±0.029	−0.098±0.059	0.177±0.054	11.42

In the simple case of $\phi=0$, we have $\hat{Y}=\hat{n}=R\hat{n}$ since the field is vertical. The rotation thus reduces to a precession of an angle ω around $\hat{n}$, mixing the s' and k' polarization components, i.e., $\hat{n}_a=\hat{n}=R\hat{n}$ and $\hat{s}_a=\hat{n}\times\hat{k}_a$, so that

$$\begin{aligned} R\hat{s}' &= \cos\omega\,\hat{s}_a+\sin\omega\,\hat{k}_a\ , \\ R\hat{k}' &= -\sin\omega\,\hat{s}_a+\cos\omega\,\hat{k}_a\ . \end{aligned} \tag{18}$$

The precession angle ω is expressed as $\omega=\mu_a\gamma\theta_p$ where $\mu_a=1.793$ is the anomalous magnetic moment of the proton, γ the Lorentz factor, and θ_p the bending angle of the scattered proton trajectory in the magnetic field. From Eq. (16) the measured transverse polarization components then reduce to

$$\begin{aligned} R\vec{P}\cdot\hat{s}_a &= \cos\omega\,P_{s'}-\sin\omega\,P_{k'}\ , \\ R\vec{P}\cdot\hat{n}_a &= P_n\ . \end{aligned} \tag{19}$$

In the general case of $\phi\neq 0$, the situation is more complicated since a radial component of the magnetic field appears and $\hat{n}$ is no longer parallel to the vertical field and becomes significantly different from $R\hat{n}$. Numerical calculations using the same tracking program that were used in the matrix generation have shown that

$$\begin{aligned} R\vec{P}\cdot\hat{s}_a &\simeq \cos\omega\,P_{s'}-\sin\omega\,P_{k'}\ , \\ R\vec{P}\cdot\hat{n}_a &\simeq P_n+\phi b P_{k'}\ , \end{aligned} \tag{20}$$

to a very good approximation in our $\theta_{\text{c.m.}},\phi$ angular range. A first-order analytical calculation using a transfer matrix formalism for spin rotation[17] has confirmed this result. In particular $b\simeq\omega\cos\theta_{\text{lab}}$ was found. The ϕ antisymmetric term $\phi b P_{k'}$ can easily be neglected since the method used for parameter extraction (see Sec. V B) integrates the data symmetrically over ϕ. Possible remaining contributions from ϕ antisymmetric terms in $P_{k'}$ are lower than 0.001. With this approximation Eq. (20) reduces to (19).

Finally the polarization components measured along the $\hat{n}_a$ and $\hat{s}_a$ axes by the polarimeter therefore essentially correspond to the spin components of the proton along the direction $\hat{n}$ and $\hat{\omega}$ at the PPT, where

$$\hat{\omega}=\cos\omega\,\hat{s}'-\sin\omega\,\hat{k}'\ . \tag{21}$$

The component along $\hat{s}_a$ is then

$$P_\omega=\cos\omega\,P_{s'}-\sin\omega\,P_{k'}\ . \tag{22}$$

At 579 MeV, ω varied from about 7.5° to 12° for $\theta_{\text{c.m.}}$ between 30° and 122°. Values are given in Table II. It can be noted that the mixing of observables within the scattering plane by the angle ω has an effect analogous to that of the Wigner rotation induced by transformations from c.m. to laboratory frame.

2. *Estimators of the asymmetries*

For each bin $(\theta_{\text{c.m.}},\phi,S^2)$ and for each k bin in θ_{C}, the Fourier estimates of the asymmetries[18] measured along the axes $\hat{n}$ and $\hat{\omega}$ are given by

$$\begin{aligned} \epsilon_{n,k} &= 2\sum_{\text{ev}}\cos\phi_{\text{C}}/N_k\ , \\ \epsilon_{\omega,k} &= -2\sum_{\text{ev}}\sin\phi_{\text{C}}/N_k\ , \end{aligned} \tag{23}$$

where the error in both cases is

$$\sigma^2(\epsilon)=2/N_k\ . \tag{24}$$

Here, the summation runs over all events in the θ_{C} bin k, N_k is the total number of events in bin k, and ϕ_{C} is the pC azimuthal angle defined in Eq. (14). The polarization components could then be found by dividing by the analyzing power, $A_{\text{C},k}$,

$$\begin{aligned} P_{n,k} &= \epsilon_{n,k}/A_{\text{C},k}\ , \\ P_{\omega,k} &= \epsilon_{\omega,k}/A_{\text{C},k}\ , \end{aligned} \tag{25}$$

with the errors

$$\sigma_k{}^2=2/(N_k A_{\text{C},k}{}^2)\ . \tag{26}$$

These pC analyzing powers were determined from a two-dimensional empirical formula fitting our previously measured data points[13,8] as a function of kinetic energy T and angle θ_{C} for the corresponding carbon thickness. This was chosen to be 7 cm for the detector-arm positions at 48° c.m. and 80° c.m., and 3 cm for the 104° c.m..

To estimate the polarization components from the entire angular range in θ_{C}, we performed a weighted mean over the estimations found in each of the $\theta_{\text{C},k}$ bins providing

$$P_n=\frac{\sum_k(\epsilon_{n,k}/A_{\text{C},k})(1/\sigma_k{}^2)}{\sum_k(1/\sigma_k{}^2)}=\frac{2\sum_{\text{all}}\cos\phi_{\text{C}}A_{\text{C}}}{\sum_{\text{all}}A_{\text{C}}{}^2} \tag{27}$$

and

$$P_\omega=\frac{-2\sum_{\text{all}}\sin\phi_{\text{C}}A_{\text{C}}}{\sum_{\text{all}}A_{\text{C}}{}^2}\ , \tag{28}$$

with

$$\sigma^2(P)=1/\sum_k(1/\sigma_k^2)=2/\sum_{\text{all}}A_C^2 . \quad (29)$$

In the analysis, the three sums in Eqs. (27)—(29) were accumulated over all carbon events for each bin in $(\theta_{\text{c.m.}},\phi,S^2)$ of the double-scattering events and the polarization components P_n and P_ω extracted. In fact a fourth sum $\sum_{\text{all}}A_C\sigma'/\sigma$ was also accumulated in order to correct for residual misalignments (see below, Sec. V A 3).

3. *Corrections for residual chamber misalignments*

In evaluating the carbon scattering asymmetries, it was also necessary to account for residual misalignments of the MWPC's due to local construction faults such as nonparallel or unequally spaced wires, etc. To a first approximation, false asymmetries arising from such faults can be estimated[13] by

$$\begin{aligned}\Delta\epsilon_s&=\Delta_s(\sigma'_C/\sigma_C) ,\\ \Delta\epsilon_n&=\Delta_n(\sigma'_C/\sigma_C) ,\end{aligned} \quad (30)$$

where σ'_C/σ_C is the logarithmic derivative of the carbon scattering cross section, $d(\ln\sigma_C)/d\theta_C$. The transverse displacements Δ_s and Δ_n can be evaluated using the "straight-through" track data taken alternatively with double-scattering events, i.e.,

$$\begin{aligned}\Delta_s&=\langle\tan\theta_C\sin\phi_C\rangle ,\\ \Delta_n&=\langle\tan\theta_C\cos\phi_C\rangle ,\end{aligned} \quad (31)$$

where the angular brackets indicate an average over all events with $\theta_C\lesssim 2.6°$. Typical values for Δ_s and Δ_n were 0.02 to 0.03°. The corrected polarization components are then given by

$$\begin{aligned}P_\omega&=-\left[2\sum_{\text{all}}A_C\sin\phi_C+\Delta_s\sum_{\text{all}}A_C\sigma'_C/\sigma_C\right]\Big/\sum_{\text{all}}A_C^2 ,\\ P_n&=\left[2\sum_{\text{all}}A_C\cos\phi_C+\Delta_n\sum_{\text{all}}A_C\sigma'_C/\sigma_C\right]\Big/\sum_{\text{all}}A_C^2 .\end{aligned} \quad (32)$$

4. *Background subtraction*

The background reactions in this experiment consisted mainly of the inelastic pp reactions:

$$pp\to\pi d ,$$

$$pp\to NN\pi ,$$

and proton reactions on the C and ^{3}He nuclei present in the PPT and the copper target cavity. Of the inelastic reactions, $pp\to\pi d$ events could be neglected since they fell outside the geometrical acceptance of the apparatus, while contamination from the πNN reaction was estimated to be less than 0.1%.

Reactions due to the various nuclei in the PPT were measured with a dummy target as already described in Sec. III C. The rate was generally small giving noise/signal ratio of about 5%. It might be interesting to point out that the background contamination is smaller than the one observed in the A_{00nn} experiment[12] performed with a very similar geometry. This is due to the corrections of the nonlinearity (see Sec. IV B 1) which allow more restrictive cuts. Following the method of Ref. 18, these events were then analyzed in the same way as the butanol events and the sums in Eqs. (27) to (29) evaluated. These were then subtracted from the corresponding butanol sums to give

$$P_n=\frac{2\left[\sum_{\text{but}}A_C\cos\phi_C-\alpha\sum_{\text{dummy}}A_C\cos\phi_C\right]}{\sum_{\text{but}}A_C^2-\alpha\sum_{\text{dummy}}A_C^2} \quad (33)$$

and a corresponding sum for P_ω. The errors then become

$$\sigma^2(P)=\frac{2\left[\sum_{\text{but}}A_C^2+\alpha^2\sum_{\text{dummy}}A_C^2\right]}{\left[\sum_{\text{but}}A_C^2-\alpha\sum_{\text{dummy}}A_C^2\right]^2} , \quad (34)$$

where the factor α is a renormalization constant which accounts for the difference in the total number of atoms in the butanol and dummy targets and the number of incident protons for the two measurements.

B. Evaluation of the spin-dependent parameters

The analysis in the previous section provided the polarizations P_n and P_ω for each bin in $\theta_{\text{c.m.}}$ and ϕ. To extract the polarization parameters from these quantities, it was first necessary to remove the dependence on angle ϕ coming from the projections of $\vec{P}_b$ and $\vec{P}_t$ onto the reaction frame of the proton, i.e. $(\hat{s},\hat{n},\hat{k})$. Let us therefore calculate Eq. (2) explicitly for the case of P_t along $\hat{Y}$ and P_b along $\hat{X}$, $\hat{Y}$, and $\hat{Z}$, treating the denominator and numerator of Eq. (2) separately.

However, a remark concerning the beam-polarization components must first be made. Because of the magnetic field surrounding the target, a

spin precession of the incident proton also occurs before it is scattered. Thus at the point of the reaction, the beam generally has a mixture of several beam components, even if it is completely polarized along one of the basis axes originally. With the vertical magnetic field, the following mixings occurred: (1) For P_b along $\hat{Y}$, no mixing occurred so that $P_{bY}=P_b$, $P_{bX}=P_{bZ}=0$ at the reaction point. (2) For P_b along $\hat{X}$ or $\hat{Z}$, a precession occurred only in the horizontal plane so that at the reaction point, $\vec{P}_b=P_{bX}\hat{X}+P_{bZ}\hat{Z}$, $P_{bY}=0$ with the P_{bX} (P_{bZ}) component being the most dominant for P_b originally along $\hat{X}$ ($\hat{Z}$). For this analysis, the "reaction" components in each case were estimated at the center of the target using the tracking-matrix generation program.

1. The denominator

Projecting out the "reaction" beam and target components onto the $(\hat{s},\hat{n},\hat{k})$ frame, the denominators of Eq. (2) become

P_b along $\hat{Y}$:

$$1+A(P_b+P_t)\cos\phi+A_{00nn}P_tP_b\cos^2\phi+A_{00ss}P_bP_t\sin^2\phi\ , \quad (35)$$

where we have used the Pauli principle implying $A_{00n0}=A_{000n}=A$, and

P_b in the $\hat{X},\hat{Z}$ plane:

$$1+A(P_t\cos\phi-P_{bX}\sin\phi)-A_{00nn}P_{bX}P_t\sin\phi\cos\phi+A_{00ss}P_tP_{bX}\sin\phi\cos\phi+A_{00ks}P_{bZ}P_t\sin\phi\ . \quad (36)$$

2. The numerator

For the spin component along $\hat{\omega}$, P_ω, the numerators are

P_b along $\hat{Y}$:

$$D_{\omega 0s0}P_b\sin\phi+K_{\omega 00s}P_t\sin\phi+M_{\omega 0ns}P_bP_t\cos\phi\sin\phi+M_{\omega 0sn}P_bP_t\sin\phi\cos\phi\ . \quad (37)$$

P_b in the $\hat{X},\hat{Z}$ plane:

$$D_{\omega 0s0}P_{bX}\cos\phi+K_{\omega 00s}P_t\sin\phi-M_{\omega 0ns}P_{bX}P_t\sin^2\phi+M_{\omega 0sn}P_{bX}P_t\cos^2\phi+D_{\omega 0k0}P_{bZ}+M_{\omega 0kn}P_{bZ}P_t\cos\phi\ , \quad (38)$$

where we have also applied parity conservation. Since $\sin\phi$ is close to 0, while the $\cos\phi$ is $\simeq 1$ in our measured range, the dominating terms in these ex-

TABLE III. Same as Table II but for the parameters P, K_{n0n0}, and D_{n00n}. Quoted errors are purely statistical.

$\theta_{\text{c.m.}}$ (deg)	P	K_{n00n}	D_{n0n0}
34	0.587±0.013	0.281±0.025	0.903±0.039
38	0.573±0.010	0.344±0.020	0.742±0.032
42	0.578±0.010	0.373±0.019	0.788±0.030
46	0.504±0.009	0.396±0.018	0.804±0.029
50	0.518±0.009	0.437±0.018	0.875±0.028
54	0.466±0.009	0.439±0.017	0.871±0.027
58	0.433±0.008	0.502±0.017	0.808±0.027
62	0.400±0.009	0.482±0.017	0.873±0.028
66	0.365±0.009	0.494±0.016	
70	0.335±0.008	0.534±0.014	
74	0.262±0.008	0.550±0.014	0.767±0.025
78	0.198±0.008	0.542±0.013	0.758±0.024
82	0.143±0.008	0.599±0.013	0.678±0.022
86	0.081±0.008	0.632±0.012	0.715±0.024
90	−0.006±0.008	0.663±0.012	0.686±0.023
94	−0.075±0.009	0.720±0.013	0.643±0.021
90	0.005±0.009	0.669±0.014	
94	−0.059±0.008	0.706±0.012	
98	−0.116±0.008	0.716±0.012	0.618±0.021
102	−0.179±0.008	0.731±0.012	0.592±0.024
106	−0.261±0.008	0.752±0.012	
110	−0.304±0.008	0.761±0.013	
114	−0.362±0.009	0.782±0.014	
118	−0.400±0.012	0.794±0.020	

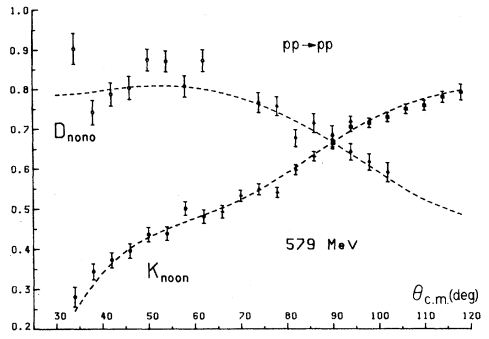

FIG. 6. D_{n0n0},K_{n00n} for pp elastic at 579 MeV as a function of the c.m. scattering angle. The three different symbol (dots, triangles, squares) correspond to the three different turntable settings used to cover the whole angular range.

pressions are $D_{\omega 0s0}$, $D_{\omega 0k0}$, $M_{\omega 0sn}$, and $M_{\omega 0kn}$. We remind the reader also that the index ω on the parameters refers to the direction defined in Eq. (21) and that

$$X_\omega \ldots = \cos\omega\, X_{s'} \ldots - \sin\omega\, X_{k'} \ldots , \tag{39}$$

where X is any polarization parameter.

For the spin component along $\hat{n}$, P_n, we similarly find using the relation $M_{n0nn}=P$

P_b along $\hat{Y}$:

$$P(1+P_bP_t\cos^2\phi)+D_{n0n0}P_b\cos\phi+K_{n00n}P_t\cos\phi + M_{n0ss}P_bP_t\sin^2\phi . \tag{40}$$

P_b in the $\hat{X},\hat{Z}$ plane:

$$P(1-P_{bX}P_t\sin\phi\cos\phi)-D_{n0n0}P_{bX}\sin\phi+K_{n00n}P_t\cos\phi + M_{n0ss}P_{bX}P_t\cos\phi\sin\phi+M_{n0ks}P_{bZ}P_t\sin\phi , \tag{41}$$

where the dominant terms involve D_{n0n0}, K_{n00n}, and P.

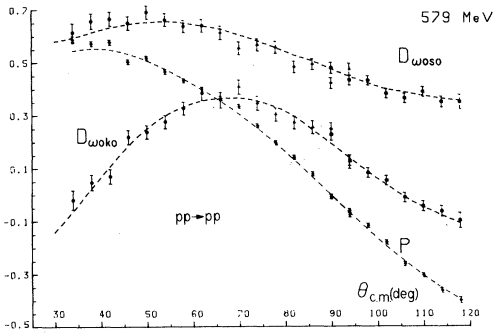

FIG. 7. P_{n000},$D_{\omega 0s0}$,$D_{\omega 0k0}$ for pp scattering at 579 MeV as a function of the c.m. scattering angle.

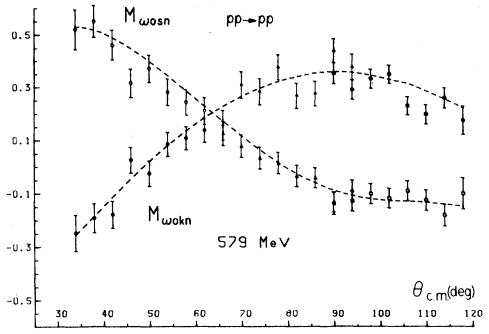

FIG. 8. $M_{\omega 0sn}$,$M_{\omega 0kn}$ for pp elastic scattering at 579 MeV as a function of the c.m. scattering angle.

3. *Extraction of the polarization parameters*

Since the parameters in the denominators given by Eqs. (35) and (36) have already been measured,[12,19] this expression could easily be evaluated for our data, so that, the numerators alone could be extracted

$$N_i = P_i \times \text{denominator} . \tag{42}$$

For this purpose, smoothed values of the spin-correlation parameters from a fit by the Saclay-Geneva PSA were used. The errors incurred by using these PSA values were negligible in comparison to the data.

Since the data were grouped into five ϕ bins symmetric about $\phi=0$, the small $\sin\phi$ terms could be canceled by adding the $\{\phi,-\phi\}$ bins, i.e.,

$$\begin{aligned} N_{i'} &= [N_i(\phi)+N_i(-\phi)]/2 , \\ N_{0'} &= N(0) , \end{aligned} \tag{43}$$

to give three bins in ϕ. This left only the dominant $\cos\phi$ terms and the residual terms in $\sin^2\phi$, M_{n0ss}, M_{s0ns}, and M_{k0ns}, which contributed very little. These were nevertheless corrected for by using the PSA predictions. The remaining parameters were then obtained by fitting the symmetrized expression in Eq. (43) for all ϕ and all P_b and P_t combinations for each separate bin in $\theta_{c.m.}$ to yield the parameters P, D_{n0n0}, K_{n00n}, $D_{\omega 0s0}$, $D_{\omega 0k0}$, $M_{\omega 0sn}$, and $M_{\omega 0kn}$.

4. *Target calibration independently of the NMR signal*

In this analysis, it was possible to check the NMR calibration of the target by exploiting the symmetry relation

$$D_{n0n0}(\theta_{c.m.})=K_{n00n}(\pi-\theta_{c.m.}) \tag{44}$$

which follows from the Pauli principle. Referring

to Table I, it can be seen that when measurements are done with both beam and target polarizations along $\hat{Y}$, one measures D_{n0n0} and K_{n00n} simultaneously. However D_{n0n0} is entirely determined by P_b whereas K_{n00n} is determined by P_t. Using the above relation around 90° c.m., then, it was possible to compare the target polarization with the better known value of the "scattered" beam polarization ($|\vec{P}_b| = 0.4165 \pm 0.0043$), i.e.,

$$P_b D_{n0n0}(\theta_{\text{c.m.}})/P_b = \alpha K_{n00n}(\pi - \theta_{\text{c.m.}}) P_{t,\text{wanted}}/P_t \ . \tag{45}$$

In this way, our desired P_t value is given by the ratio of the P_t value derived from the NMR calibration and the normalization factor α,

$$P_{t,\text{wanted}} = P_t/\alpha \ . \tag{46}$$

In practice α was determined by fitting $D_{n0n0}(\theta_{\text{c.m.}})$ to $K_{n00n}(\pi - \theta_{\text{c.m.}})$ around 90° c.m. This method is sensitive to the sum of the positive and negative polarization values ($|P_{t+} + P_{t-}|$). The relative accuracy obtained was $\lesssim 3\%$ including systematic uncertainties, an accuracy comparable to the NMR techniques. This provided us with secure D_{n0n0} and K_{n00n} measurements. In addition, since K_{n00n} is always measured for each P_b orientation (see Table I), this allows an extensive control of the P_t values independently of the NMR signal.

VI. RESULTS AND CONCLUSIONS

The experimental results obtained for the spin-dependent parameters are given in Tables II and III along with their statistical errors. The mixing angle ω for each $\theta_{\text{c.m.}}$ bin is given in Table II also. Figures 6 to 8 plot the results along with fits (dotted lines) from the Saclay-Geneva phase shift analysis performed at a fixed energy of 579 MeV. In addition to the points from this experiment, these fits also included previously measured data at small angles,[15] and spin-correlation parameters[12,19] measured in the same angular range. As can be seen, the points from this experiment are fit very well indicating good consistency with the other measurements. As well, note that the relation $P(\theta_{\text{c.m.}}) = -P(\pi - \theta_{\text{c.m.}})$ required by the Pauli principle is very well reproduced by the data.

The most striking feature of these data, however, is their very large magnitude. The three-spin parameter $M_{\omega 0sn}$, for example, reaches a high of 0.55, comparable to that of P indicating some rather strong spin effects in pp scattering. It is interesting to note, as well, the astonishingly smooth angular dependence of the parameters in this range. This is in sharp contrast to their behavior at small angles[15] where the effect of one-pion exchange dominates. The Coulomb interaction also becomes important. Our data should be compared to the rather extensive set of two-spin measurements at 647 and 800 MeV at LAMPF (Ref. 20), which show equally large spin effects, and the Argonne data at 6 GeV/c (Ref. 21), which include three-spin parameters although measured with rather large statistical errors.

The relative statistical precision of the parameters was determined, as we have already remarked, by their determination factors in Eq. (2). The three-spin parameters were the least well determined with an error of about ± 0.05. This is a more than useful precision, however, and marks the first time this has been achieved for a three-spin parameter. As mentioned in Ref. 8, these quantities were necessary for an unambiguous amplitude reconstruction at 90° c.m.

The systematic errors were of two types: (1) multiplicative, due to uncertainties in the determination factors and (2) additive, due to biases in the experimental apparatus. Table IV lists the contributions involved multiplicatively in the determination of the parameters. These were mainly due to uncertainties in the beam and target polarizations and carbon analyzing power A_C. Their estimated relative uncertainties are listed in the last column. Table V shows how the determination factors affect the normalization of the various observables. The quoted errors represent the total relative systematic uncertainty for the concerned parameter. The data taken between 34° c.m. and 62° c.m., and from 90° c.m. to 118° c.m. have some larger errors since they were

TABLE IV. Determination factors for the parameters.

Normalization	Parameter	Meaning	Relative uncertainty
$r_n(1)$	$A_c P_{b,\text{scatt}}$	Carbon calibration	1–2 %
$r_n(2)$	$P_{b,\text{scatt}}$	Calibration scattered beam	1%
$r_n(3)$	$P_{b,\text{acc}}/P_{b,\text{scatt}}$	Calibration accelerated beam	3%
$r_n(4)$	P_t	Calibration target polarization	5%

TABLE V. Normalizations of the parameters.

Parameter	Normalization	Relative uncertainty
P	$r_n(1)/r_n(2)$	2–3 %
K_{n00n}	$r_n(1)r_n(4)/r_n(2)$	6–7 %
D	$r_n(1)$	1–2 %
$D_{n0n0}(34°–62°)$, $D_{\omega 0s0}(90°–118°)$	$r_n(1)r_n(3)$	3–4 %
M	$r_n(1)r_n(4)$	6%
$M_{\omega 0sn}(90°–118°)$	$r_n(1)r_n(3)r_n(4)$	7–8 %

taken with the "accelerated" beam where the polarization is less well known.

The polarizations P_ω and P_n measured along the ω and n axes may also contain additive biases b_ω, b_n, due to nonuniform MWPC efficiencies in ϕ, noncentral passage through the polarimeter with nonsymmetric absorption and multiple scattering. The bias along ω, b_ω (which does not depend on P_b or P_t) cancels out when combining data of opposite beam polarization. Therefore, $D_{\omega 0s0}$, $D_{\omega 0k0}$, $M_{\omega 0sn}$, and $M_{\omega 0kn}$ are free of any additive bias. On the other hand, the bias along n directly affects the polarization parameter P no matter what data combination is made, as can be seen from Table I. However, b_n can be estimated by looking at how the polarization P passes through 0 at 90° c.m.; b_n was found consistent with zero to within an accuracy of about 1 standard deviation. Since the 90° c.m. bin was in the border regions of the polarimeter where bias effects are expected to be largest, the overall bias comes out to be smaller than the statistical error.

Systematic errors due to nonsymmetric absorption in the polarimeter and uncertainties in the energy of the analyzing pC scattering reaction were also considered. This is particularly crucial for the large angle ($\theta_{\text{c.m.}} \geq 114°$) measurements since scattered proton has a kinetic energy below 165 MeV and is in a region where the carbon analyzing power varies rapidly with energy [a 5-MeV change in kinetic energy results in a $\Delta(\text{observ})/\text{observ}=5\%$ at 118° c.m., 3% at 114° c.m., and $<1\%$ for all other angles].

Finally, we note that the D and M parameters above 90° can be related to certain parameters below 90° if the Pauli principle is invoked. More explicitly, these are

$$\begin{aligned} K_{n00n}(\theta) &= D_{n0n0}(\pi-\theta)\ , \\ K_{0\omega s0}(\theta) &= D_{\omega 0s0}(\pi-\theta)\ , \\ K_{0\omega k0}(\theta) &= -D_{\omega 0k0}(\pi-\theta)\ , \\ N_{0\omega sn}(\theta) &= -M_{\omega 0sn}(\pi-\theta)\ , \\ N_{0\omega kn}(\theta) &= M_{\omega 0kn}(\pi-\theta)\ . \end{aligned} \tag{47}$$

If these are used, the ensemble of points may then be interpreted as providing information on 11 polarization parameters between 62° and 90°. These parameters, along with the differential cross section and the spin correlation parameters A_{00nn}, A_{00sk}, and A_{00kk} from earlier measurements, in fact, form the basis for a "complete" experiment.[9] As well, the large number of parameters also made possible, a reconstruction of the time-reversal violating amplitude,[22,8] providing the first model-independent upper limit on T violation in the strong interaction. For angles below 62° c.m. where less observables were at our disposal [because Eq. (47) could not be used], an unambiguous reconstruction of the amplitudes has also been possible[8] giving extremely interesting results down to a rather small scattering angle $\theta_{\text{c.m.}}$ of 38°.

ACKNOWLEDGMENTS

We would like to thank the Swiss Institute for Nuclear Research for its valuable technical assistance during the experiment and express our special gratitude to Professor J. P. Blaser, its director. We would also like to thank Professor R. Mermod for his constant encouragement throughout this work and the technical staff of the University of Geneva. This work was supported by the Swiss National Science Foundation and the Convention Intercantonale d'Enseignement du 3eme cycle de la Physique en Suisse Romande.

*Present address: University of California, Physics Department, Irvine, CA 92717.

[1]A. W. Thomas, Reports Nos. TH-3368-CERN and TRI-PP-82-29 (unpublished).

[2]R. Vinh Mau, Nucl. Phys. A374, 3C (1982).

[3]R. Vinh Mau, in *From Collective States to Quarks in Nuclei*, No. 137 of *Lectures Notes in Physics*, edited by H. Arenhovel and A. Sarius (Springer, Berlin, 1981).

[4]M. Lacombe, B. Loiseau, R. Vinh Mau, J. Cote, P. Pires, and R. de Tourreil, Phys. Rev. C 23, 2405 (1981).

[5]E. Aprile-Giboni, Ph.D. thesis No. 2066, University of Geneva, 1982 (unpublished).

[6]L. Puzikov, R. Ryndin, and J. Smorodinsky, Nucl. Phys. 3, 436 (1957).

[7]D. Besset, B. Favier, L. G. Greeniaus, R. Hess, D. Rapin, D. W. Werren, and C. Weddigen, Nucl. Instrum. Methods 148, 129 (1978).

[8]R. Hausammann, Ph.D. thesis No. 2038, University of Geneva, 1982 (unpublished).

[9]E. Aprile, C. Eisenegger, R. Hausammann, E. Heer, R. Hess, C. Lechanoine-Leluc, W. R. Leo, S. Morenzoni, Y. Onel, D. Rapin, and S. Mango, Phys. Rev. Lett. 46, 1047 (1981).

[10]J. Bystricky, F. Lehar, and P. Winternitz, J. Phys. (Paris) 39, 1 (1978).

[11]A. Bohr, Nucl. Phys. 10, 486 (1959).

[12]D. Besset, Q. H. Do, B. Favier, R. Hausammann, E. Heer, R. Hess, C. Lechanoine, W. R. Leo, D. Rapin, D. W. Werren, Ch. Weddigen, J. M. Cameron, S. Jaccard, and S. Mango, Nucl. Phys. A345, 435 (1980).

[13]D. Besset, Q. H. Do, B. Favier, L. G. Greeniaus, R. Hess, C. Lechanoine, D. Rapin, D. W. Werren, and Ch. Weddigen, Nucl. Instrum. Methods 166, 377 (1979); E. Aprile, R. Hausammann, E. Heer, R. Hess, C. Lechanoine-Leluc, W. R. Leo, S. Morenzoni, Y. Onel, and D. Rapin, *ibid.* (to be published).

[14]D. Besset, Q. H. Do, B. Favier, L. G. Greeniaus, E. Heer, R. Hess, C. Lechanoine-Leluc, D. Rapin, D. W. Werren, M. Daum, S. Mango, E. Steiner, G. Vecsey, and Ch. Weddigen, Nucl. Instrum. Methods 184, 365 (1981).

[15]D. Besset, Q. H. Do, B. Favier, L. G. Greeniaus, R. Hess, C. Lechanoine, D. Rapin, D. W. Werren, and Ch. Weddigen, Phys. Rev. Lett. 21, 580 (1980).

[16]E. Aprile, R. Hausammann, E. Heer, R. Hess, C. Lechanoine, W. R. Leo, S. Morenzoni, Y. Onel, and D. Rapin, CERN Yellow Report No. 81-07, p. 124 (unpublished).

[17]D. Rapin, R. Hess, J. C. Nikles, and D. W. Werren, in *Cyclotrons—1972,* Proceedings of the Sixth International Cyclotron Conference, Vancouver, edited by J. J. Burgerson and A. Strathdee (AIP, New York, 1972), p. 425.

[18]D. Besset, B. Favier, L. G. Greeniaus, R. Hess, C. Lechanoine, D. Rapin, and D. W. Werren, Nucl. Instrum. Methods 166, 515 (1979).

[19]E. Aprile, R. Hausammann, E. Heer, R. Hess, S. Jaccard, W. Leo, Y. Onel, S. Mango, and D. Rapin, in *Polarization Phenomena in Nuclear Physics—1980,* proceedings of the Fifth International Symposium, Santa Fe, edited by G. G. Ohlson, R. E. Brown, N. Jarmie, M. W. McNaughton, and G. M. Hale (AIP, New York, 1981).

[20]M. W. McNaughton, B. E. Bonner, E. W. Hoffman, O. B. van Dyck, C. L. Hollas, P. J. Riley, K. H. McNaughton, K. Imai, K. Toshioka, J. Roberts, S. E. Turpin, B. Aas, and A. Rahbar, Phys. Rev. C 26, 249 (1982); M. W. McNaughton, E. P. Chamberlin, J. J. Jarmer, N. S. King, H. B. Willard, and E. Winkelman, *ibid.* 25, 2107 (1982); M. W. McNaughton, B. E. Bonner, W. D. Cornelius, E. W. Hoffman, O. B. van Dyck, R. L. York, R. D. Ransome, C. L. Hollas, P. J. Riley, and K. Toshioka, *ibid.* 25, 1967 (1982).

[21]A. Beretvas, D. Miller, I. P. Auer, R. Giese, D. Hill, K. Nield, P. Rynes, B. Sandler, Y. Watanabe, and A. Yokosawa, Phys. Rev. D 20, 21 (1979).

[22]E. Aprile, R. Hausammann, E. Heer, R. Hess, C. Lechanoine-Leluc, W. R. Leo, S. Morenzoni, Y. Onel, and D. Rapin, Phys. Rev. Lett. 47, 1360 (1981).